Electron emission from single-electron capture with simultaneous single-ionization reactions in 30-keV/u He²⁺-on-argon collisions

X. Ma,[1,*] R. T. Zhang,[1,2] S. F. Zhang,[1] X. L. Zhu,[1] W. T. Feng,[1] D. L. Guo,[1,2] B. Li,[1] H. P. Liu,[1]
C. Y. Li,[3] J. G. Wang,[3] S. C. Yan,[1,2] P. J. Zhang,[1,2] and Q. Wang[1,2]

[1]*Institute of Modern Physics, Chinese Academy of Sciences, Lanzhou 730000, China*
[2]*Graduate University of Chinese Academy of Sciences, Beijing 100049, China*
[3]*Institute of Applied Physics and Computational Mathematics, Beijing 100088, China*
(Received 16 February 2011; published 20 May 2011)

Electron emission from the single-electron capture with simultaneous single ionization in 30 keV/u He²⁺ on argon was investigated using a reaction microscope, providing the electron energy spectra and momentum distributions. Intensive peaks for electrons with near-zero kinetic energies have been observed. It is demonstrated that mechanisms contributing to the electron emission include direct transfer ionization (DTI), double-electron capture with autoionization (DECA), and single-electron capture with autoionization (SECA) of target. Comparison of resonance energies shows that Ar⁺ ions in SECA decay mainly through the $3s3p^53d$ states by emitting Auger electrons, and He** in DECA decay through the $2l2l'$ states. The dependence of electron emission on the transverse momentum exchange has been studied. In the transfer ionization channel studied here, the DTI process dominates the electron emission, and no saddle point electron mechanism has been found.

I. INTRODUCTION

The atomic collision ionization by charged particles has been an attractive subject due to both its importance in fundamental physics and its application in many fields, such as laboratory and astrophysical plasmas, radiation physics, and so on. In recent decades, single ionization of H and He atoms has been studied in detail experimentally as well as theoretically from intermediate [1–3] to relativistic [4,5] collision energies. Recently, interest in ionization processes involving two and more active electrons is increasing with the development of coincident measurements and reaction microscope techniques. When a bare projectile collides with an atomic target, the two electron processes include double-electron capture (DEC), double ionization (DI), transfer ionization (TI), and single ionization (SI) of the target accompanied by target excitation. The studies of these reactions are essential to understand the role of electron correlation [6,7] in these processes.

Transfer ionization at low incident energies was investigated in detail using protons and He²⁺ as projectiles. In the incident energy range of 150 keV–1.4 MeV, Mergel *et al.* [8] studied the transfer ionization in *p*-He collisions by using the cold target recoil ion momentum spectroscopy (COLTRIMS) [9,10]. From the measured fourfold differential cross sections, independent two-step processes of one-electron capture with ionization of target and the electron-electron Thomas scattering are clearly distinguished. In a later publication [11], Mergel *et al.* studied the electron emissions in the scattering plane and in the backward direction; they argued that the strong correlations in the He ground-state momentum wave function played a role and concluded that it is the evidence of a new transfer ionization mechanism. Abdallah *et al.* [12] measured momentum distributions of continuum electrons emitted in the impact of slow He¹⁺ and He²⁺ ions on He. Their experimental results showed that the electrons are concentrated

in the collision plane and their distributions have a structure of a π-orbital shape. Thus, they proposed that the promotion of π-orbital electrons contributes dominantly to the low-energy continuum electron production. Furthermore, Schmidt *et al.* [13] investigated the electron-emission pattern produced in the He²⁺ + He collision by kinematically complete measurements at projectile velocities between 0.6 and 1.06 a.u. Their data demonstrated that the molecular orbital (MO) promotion provides a good description of the reaction dynamics, and the symmetry of the initially populated MOs is preserved upon promotion of the electron to the continuum.

For heavier atoms impacted by bare light ions, total and partial cross sections have been available for a long time (for example, see [14,15]), but highly differential experimental data are still scarce. Moretto-Capelle *et al.* [16] studied electron emission at 35° in coincidence with recoil ions in the He²⁺ + Ar collision at an incident energy of 12.5 keV/u. The electron energy was determined by an electrostatic analyzer, and only the electrons with energies larger than 10 eV were detected. Their electron energy spectrum had a broad smooth distribution above 10 eV and showed peak structures at around 60 eV, which is due to double-electron capture into the projectile excited states. The authors concluded that the TI is important in the production of continuum electrons, and for two-electron processes the exothermic TI reaction is dominant over the autoionization process. Vikor *et al.* [17] measured the cusp electron emission in He²⁺-on-Ar collisions at 25–250 keV/u and found that TI and the electron capture to the continuum contribute to the cusp electrons. Fregenal *et al.* [18] investigated double-electron capture with simultaneous ionization in He²⁺ on Ar collisions at 25 keV/u by measuring the electron energy at different emission angles in coincidence with the neutral exit projectiles. They clearly observed the cusp electron in this reaction channel. Godunov *et al.* [19] found that fully differential cross sections of transfer ionization is sensitive to details of the electron correlations in target atom and that backward electron emission reveals the ground-state electron correlations of helium. However, no information has

---

*x.ma@impcas.ac.cn

been available concerning the dependence of the electron emission on the momentum transfer for the transfer ionization reaction in He^{2+} on Ar collisions. We have performed a series of kinematically complete experiments for He^{2+} impacting on Ar with incident energies of 30 keV/u and 60 keV/u and identified various reaction channels. In this paper, we focus on the electron emission from the single-electron capture with simultaneous ionization process in the collision of He^{2+} on Ar target at incident velocity near 1 a.u. and analyze main ionization mechanisms.

Atomic units (a.u.) will be used throughout unless indicated otherwise.

II. EXPERIMENT

The experiment was performed at the Institute of Modern Physics, Chinese Academy of Sciences, Lanzhou, China, where a dedicated beam line for atomic physics studies is equipped at the 320-kV platform for research with highly charged ions [20]. A recoil ion momentum spectrometer [21] was first constructed and employed to study the electron-capture processes [22]. Later on, an electron detector and a pair of Helmholtz coils were installed to enable collection with high efficiency and analysis of the emitted electrons in collisions. Details of the accelerator system and the experimental terminal are shown in Fig. 1.

The working principle of the reaction microscope has been described in detail in [9,10]. In brief, the reaction microscope has a two-stage supersonic gas jet. Whenever necessary, the gas can be precooled down to 77 K before expansion. The target gas flows through a 0.03-mm nozzle and is picked up by two skimmers with 0.4-mm apertures; the diameter of the atomic beam at the interaction zone is about 2 mm. The ions produced in the electron cyclotron resonance (ECR) ion source (ECRIS in Fig. 1) are first charge selected by an analyzing magnet and then accelerated to the desired energy when they leave the high-voltage platform. The ion beam is collimated before entering the collision chamber by two sets of four-jaw adjustable slits at a distance of 3.2 m. Several sets of electrostatic deflectors are installed in front of the collision zone to steer and clean the beam. The He^{2+} projectiles collide with the atomic argon at the center of the spectrometer. The

produced recoil ions and electrons are extracted perpendicular to the projectile and jet beam direction by a weak electric field of 1.8 V/cm. Then they pass through field-free drift tubes and are finally directed to the two individual time- and position-sensitive detectors (PSD-R and PSD-e). The charge states of projectiles are analyzed by an electrostatic deflector downstream of the collision center. The primary beam is collected by a Faraday cup, and the charge-changed ions are directed to a position sensitive detector (PSD-P). All position-sensitive detectors are built as a combination of the microchannel plate (MCP) with the standard delay line anode [23]. The information on the position and timing is recorded event by event by a data acquisition system based on the PXI electronics. In the offline data analysis, all three components of the momentum vectors of the recoil ions and electrons can be reconstructed according to the acquired time and position information. The magnetic field to force the electrons to move on spiral trajectories from collision zone to the detector is 10.8 Gauss. The electron energy (E_e) resolution varies with its kinetic energy. For example, the estimated energy resolution is better than 0.3 eV for $E_e < 1$ eV and is about 1 eV for E_e of 10 eV. The momentum resolution of the recoil ions and electrons for the spectrometer has been investigated in detail [24]. Assuming the maximum value of the Cartesian component is 15 a.u., the momentum resolutions of the three components of recoil ion momentum have been estimated to be $\Delta P_{R,X} \leqslant 0.20$ a.u., $\Delta P_{R,Y} \leqslant 1.50$ a.u., and $\Delta P_{R,Z} \leqslant 0.74$ a.u., respectively.

In the present studies, measurement has been carried out with triple coincidence between recoil ion, emitted electron, and scattered projectile. Thus, pure electron-capture channels have been discarded. Figure 2 shows a typical two-dimensional spectrum recorded in the experiment. Here, the vertical axis is the time of flight of the recoil ions (top: Ar^{2+}) and the horizontal axis is the projectile position corresponding to its final charge state. From the charge conservation, the highlighted areas can be assigned to various reaction channels. For example, the areas labeled with (a), (b), and (c) represent
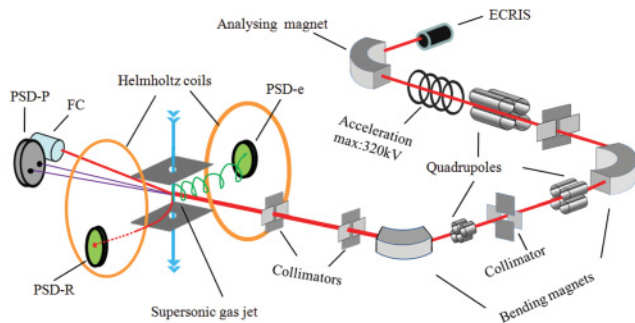

FIG. 1. (Color online) An overview of the experimental setup at the 320-kV platform for research with highly charged ions. PSD represents the microchannel plate position sensitive detector (the suffixes -R, -e, and -P corresponding to recoil ion, electron, and projectile detectors), and FC represents the Faraday cup.
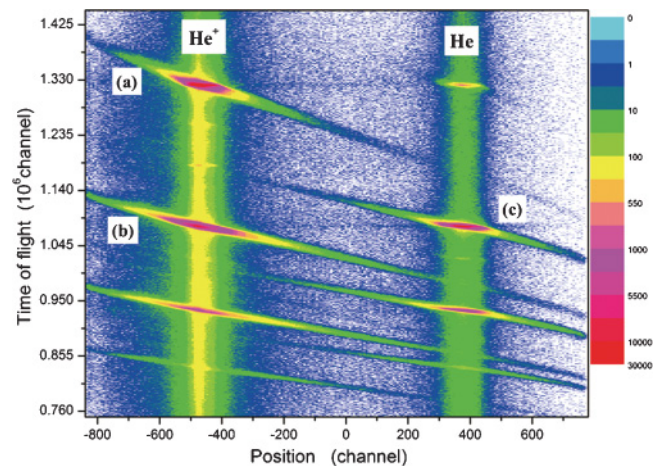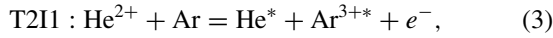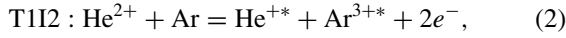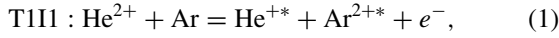

FIG. 2. (Color online) Typical two-dimensional spectrum of time of flight of the recoil ions (vertical axis) versus the scattered ion position (horizontal axis). From top to bottom, the recoil ions are Ar^{2+}, Ar^{3+}, Ar^{4+}, and Ar^{5+}. [See Eqs. (1)–(3).]

three transfer ionization channels, which can be described as following:

$$T1I1 : He^{2+} + Ar = He^{+*} + Ar^{2+*} + e^-, \qquad (1)$$

$$T1I2 : He^{2+} + Ar = He^{+*} + Ar^{3+*} + 2e^-, \qquad (2)$$

$$T2I1 : He^{2+} + Ar = He^* + Ar^{3+*} + e^-, \qquad (3)$$

where an asterisk indicates that ions can be in excited states, and TmIn represents that m electron(s) is transferred to the projectile and n electron(s) is ionized to the continuum. The charge states of recoil ions of up to five (Ar^{5+}) have been observed at the present incident energy. One should note that the wings of the areas extending to left and right sides in Fig. 2 reflect the scattering angles. When the processes with more target electrons are removed, collisions are violent and the projectiles are scattered far off the primary directions (close collisions). Extensions of the position areas of He^+ and He^0 on the detector actually overlap, but the events can be singled out in the data analysis in the two-dimensional plot as shown in Fig. 2. The cutoff of the wings at the left or right edge is due to the effective size of the projectile detector.

By setting conditions in the data-analysis procedure for the areas of interest in Fig. 2, each reaction channel can be sorted out. Thus, all differential spectra in this reaction channel can be obtained. In the present paper, we select the T1I1 transfer ionization channel and analyze the electron-emission mechanisms. Since the jet target density is not easy to determine accurately, the cross sections in the present work are calculated by normalizing the data to the values published by Dubois [14], and only the statistical errors are presented.

III. RESULTS AND DISCUSSION

In the following discussion, we employ two coordinate systems. One is the laboratory system (X, Y, Z), where the Z axis is defined by the projectile direction, the Y axis is antiparallel to the jet beam direction, and the X axis is the direction of extraction of recoil ions (right-hand system). The other one is the scattering system (x, y, z), where the z axis is again the projectile direction and the x axis is defined by the transverse momentum of the recoil ion after collisions (also a right-hand system). Here the transverse momentum of recoil ions ($P_{R,\perp}$) is perpendicular to the beam axis and defined as $P_{R,\perp} = \sqrt{P_{R,X}^2 + P_{R,Y}^2}$. It is clear that all events recorded in the laboratory system can be transformed into the scattering system (x, y, z). The scattering plane is defined by the initial momentum vector P_0 (z axis) of the incident projectile and the transverse momentum vector $P_{R,\perp}$ of the recoil ion (x axis). In the laboratory frame, this plane is randomly rotating around the incident direction from collision to collision. The electron momentum distribution has a rotational symmetry in the laboratory frame, but it only has a mirror symmetry with respect to the scattering plane. Projections of the electron distribution onto the scattering plane have been termed "top view" in literature [12,13]. In the present paper, we follow the same notations.

The top view of the electron momentum distribution is shown in Fig. 3. In this presentation, the target nucleus is located at (0, 0) and the projectile nucleus is at (1.1, 0). The recoil ion always moves upward according to the definition.
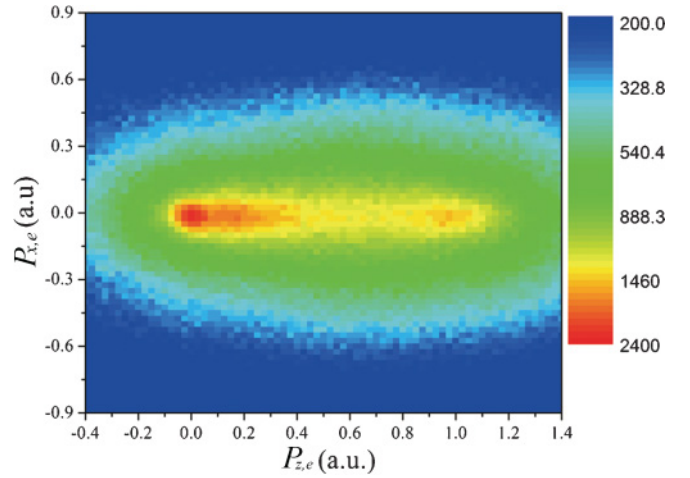

FIG. 3. (Color online) The electron momentum distribution in the scattering plane. The horizontal axis is parallel to projectile incident direction. The recoil ion moves always upward.

Apparently, the electrons are mainly concentrated between the two nuclei along the projectile direction in the velocity space. Intensive low-energy electrons were observed (momentum less than 0.2 a.u.), and most of the electrons have very small transverse momentum (within $P_{e,\perp} = \pm 0.1$ a.u., both in x and y directions). In contrast to the results of symmetric He^{2+}-on-He collisions [12,13], where a local minimum with a near-zero transverse momentum in the electron distribution was found, our results show a fully filled area and a nearly upward and downward symmetry (x direction). However, there is a shallow and wide valley between the two nuclei for $P_{ze} = 0.4 - 0.8$ a.u. This was not observed in previous studies on symmetric systems (e.g., He^{2+} on He) at similar incident velocities. The electron momentum pattern in Fig. 3 does not show any indication that the electrons are produced from the molecular orbital promotion (π or σ orbitals).

Olson [25–27] proposed the so-called saddle point (SP) mechanism for the ionization dynamics in slow ion-atom collisions based on the classical Monte Carlo calculations. Some efforts have been made to search for SP electrons also in transfer ionization processes [28]. According to the SP mechanism, the SP electron in TI should have a velocity of $v_e^{SP} = v_P \frac{1}{1+\sqrt{Z_P/Z_T}}$, where $Z_P(Z_T)$ is the final charge state of the projectile (target), respectively. In our case, the SP electrons should be found at $v_e^{SP} = 0.64$ a.u. From the electron momentum distribution pattern in Fig. 3, there only appears the shallow and wide minimum, and no evidence of the SP electrons can be concluded.

The total electron energy spectrum is shown in Fig. 4. In the present experiment, the maximum electron momentum perpendicular to the magnetic field that could be measured is 2 a.u., so the maximum electron energy corresponds to less than 80 eV. The electron energy has a broad distribution. Low-energy electrons ($E_e < 1$ eV) are very intense. The intensity decreases rapidly with increasing electron energy. Compared to the electron-energy distributions in high-energy ion-atom collisions [29,30], we find the following three characteristics: (i) The global dependences of the curves on the electron energy in both cases are quite similar, namely, smooth distribution
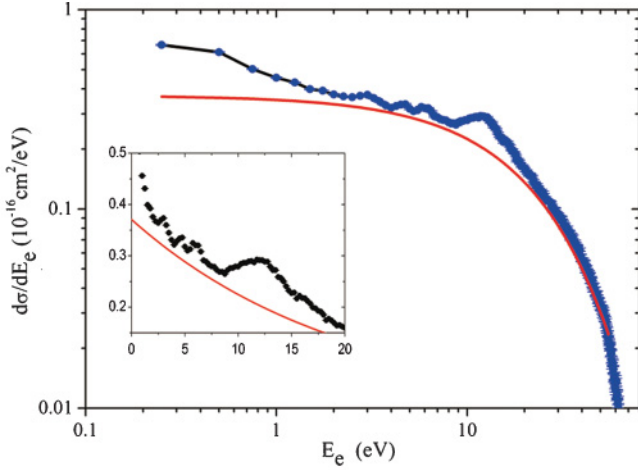
FIG. 4. (Color online) Total electron energy spectrum in the laboratory frame. The red solid line is a fit to the smooth contribution for the background subtraction. The insert shows the resonance structures.
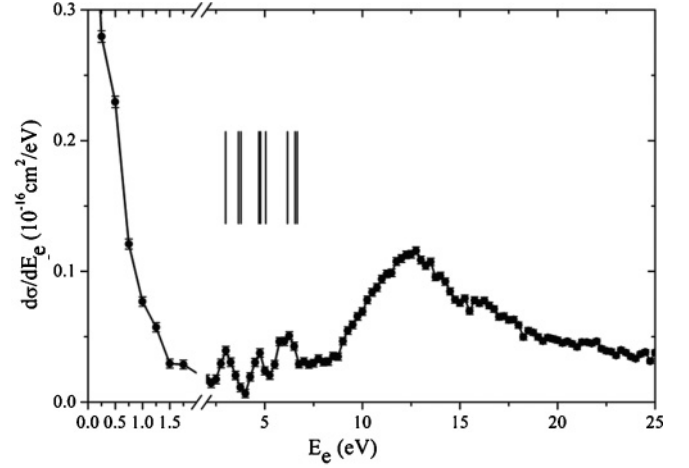

FIG. 5. Resonance structures in the electron-energy spectrum obtained from the continuum background subtraction in the laboratory frame (see Fig. 4). The vertical lines indicate the calculated Auger transitions, which are listed in Table I.

with a sharp decrease for the electron energies above 10 eV (on double log-scale). (ii) There are some resonance structures for electron energies of less than 20 eV; see the insert in Fig. 4. (iii) The intensity of the very-low-energy electrons (less than 1 eV) is much higher in the present work, while it is relatively flat or even drops in the case of pure ionization. It is believed that the smooth continuum contributions in the electron-energy spectrum is from the direct ionization of the target electron with the simultaneous single-electron capture (DTI), in which most of the electrons are localized in the continuum states of the target and lie at lower energies.

The resonance structures can be shown in a more clear way by subtracting the smooth background (DTI contribution). The background fitting is shown by the red solid line in Fig. 4, and the tailored spectrum is shown in Fig. 5. There can be two ways to produce the resonance structures. One way is that when one electron is captured into the projectile, the argon ion is left in the autoionization states and then the ion decays via the emission of Auger electron, here called SECA. Theoretical calculations indicate that the removal of one inner-shell electron, such as $1s$, $2s$, $2p$, or $3s$, can form autoionization states. Since the structures appear at low energy range (less than 20 eV), we find that whenever one $3s$ electron

is transferred and one $3p$ electron is excited into nl orbital ($3d$, $4s$ and other higher excited), the resulting autoionization states $Ar^+([Ne]3s3p^5nl)$ can decay into Ar^{2+} ($[Ne]3s^23p^4$) by emitting Auger electrons in the energy range of ~ 1.0–20.0 eV; here [Ne] denotes the inner shell $1s^22s^22p^6$. These transitions form the structures are shown in Fig. 5. In Table I, a part of the possible autoionization states has been given, which corresponds in Fig. 5 to the three peaks in the energy region of 2–7 eV. The broad peak at around 13 eV is due to the overlap of several closely spaced Auger transitions including Ar^+ ($[Ne]3s3p^5nl$, $nl = 3d$, $4s$, $4p$, $4d$). It is interesting to note that Ar^+ ($[Ne]3s3p^6$) cannot decay by the Auger process, and Ar^+ ($[Ne]3s3p^5nl$) involves three active electrons in the capture process. Up to now, we cannot be sure what role the electron correlations play, and we will address this in the future. The intensive contributions at near-zero electron energy in Fig. 5 are from the incomplete background subtraction. This means that these electrons are produced from the DTI processes.

The other way to produce the resonance structures is the autoionization decay of doubly excited states, which are formed in the double-electron capture into the projectile (DECA). Due to the fast movement of the projectile, the electrons emitted from the projectiles will have different

TABLE I. Calculated Auger transitions from the autoionizing target Ar^{+**} ions. [Ne] denotes $1s^22s^22p^2_{1/2}2p^4_{3/2}$ and J is the total angular momentum.

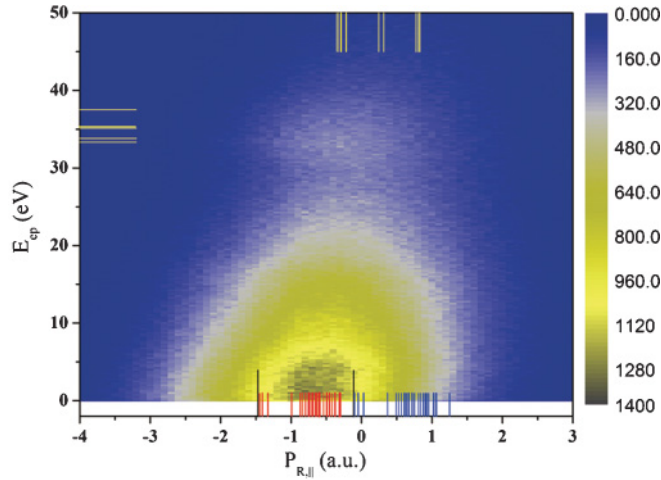| Autoionization state	Auger final state	Auger electron energy (eV)	Auger rate (s^{-1})
$[Ne]3s3p^2_{1/2}3p^3_{3/2}3d_{3/2}\ J = 7/2$	$[Ne]3s^23p^2_{1/2}3p^2_{3/2}\ J = 0$	2.99	3.03×10^{11}
$[Ne]3s3p^2_{1/2}3p^3_{3/2}4s\ J = 3/2$	$[Ne]3s^23p^2_{1/2}3p^2_{3/2}\ J = 0$	3.65	8.79×10^{13}
$[Ne]3s3p^1_{1/2}3p^4_{3/2}4s\ J = 1/2$	$[Ne]3s^23p^2_{1/2}3p^2_{3/2}\ J = 0$	3.77	9.15×10^{13}
$[Ne]3s3p^2_{1/2}3p^3_{3/2}3d_{5/2}\ J = 7/2$	$[Ne]3s^23p^2_{1/2}3p^2_{3/2}\ J = 0$	4.70	3.66×10^{13}
$[Ne]3s3p^1_{1/2}3p^4_{3/2}3d_{5/2}\ J = 5/2$	$[Ne]3s^23p^2_{1/2}3p^2_{3/2}\ J = 0$	4.78	3.14×10^{13}
$[Ne]3s3p^1_{1/2}3p^4_{3/2}3d_{5/2}\ J = 5/2$	$[Ne]3s^23p^2_{1/2}3p^2_{3/2}\ J = 0$	5.05	1.14×10^{12}
$[Ne]3s3p^1_{1/2}3p^4_{3/2}3d_{3/2}\ J = 3/2$	$[Ne]3s^23p^1_{1/2}3p^3_{3/2}\ J = 2$	6.16	4.19×10^{11}
$[Ne]3s3p^2_{1/2}3p^3_{3/2}4s\ J = 3/2$	$[Ne]3s^23p^1_{1/2}3p^3_{3/2}\ J = 2$	6.55	4.09×10^{14}
$[Ne]3s3p^1_{1/2}3p^4_{3/2}4s\ J = 1/2$	$[Ne]3s^23p^1_{1/2}3p^3_{3/2}\ J = 2$	6.66	4.26×10^{14}

FIG. 6. (Color online) The two-dimensional plot for the electron energy E_{ep} in the projectile frame versus the recoil longitudinal momenta. The horizontal lines indicate the Auger transition energies from the doubly excited states. The vertical lines in the upper part correspond to the recoil ion longitudinal momenta $P_{R,\parallel}$ for DECA. The vertical lines at the bottom represent the $P_{R,\parallel}$ for DTI. The corresponding values are listed in Table II.

energies at different observation angles in the laboratory frame. However, these electrons should have definite energies in the projectile frame. We transformed the data measured in the laboratory frame to the projectile frame. The energy data are presented in a two-dimensional plot in Fig. 6, where the horizontal axis is the recoil ion longitudinal momentum $P_{R,\parallel}$ and the vertical axis is the electron kinetic energy in the projectile frame (E_{ep}). Obviously, there is a broad resonance at around 34 eV which extends mainly from 32 to 40 eV. This indicates that the Auger transitions from the He doubly excited

$2l2l'$ states to the ground state contribute dominantly (see the short horizontal solid lines in the upper left part of Fig. 6). The Auger transition energies of the $2s^2(^1S_0)$, $2s2p$ ($^3P_{2,1,0}$), $2s2p$ ($^1P_1$), $2p^2(^3P_{2,1,0})$, $2p^2(^1D_2)$, and $2p^2(^1S_0)$ states are 33.3, 33.8, 35.3, 35.1, 35.3, and 37.5 eV, respectively. They cannot be resolved experimentally. (The transition lines are also shown in the energy spectrum in Fig. 7.)

For the double-electron capture process, the recoil ion longitudinal momentum can be calculated for different intermediate states,

$$P_{R,\parallel} = -\frac{Q}{v_P} - v_p, \qquad (4)$$

where Q is the change of the binding energies of active electrons and v_P is the projectile velocity. The yellow vertical solid lines in the upper part of Fig. 6 represent the corresponding longitudinal momenta for two electrons captured into $2s^2(^1S_0)$, $2s2p(^3P_{2,1,0})$, $2s2p(^1P_1)$, $2p^2(^3P_{2,1,0})$, $2p^2(^1D_2)$, and $2p^2(^1S_0)$ states ($2l2l'$), respectively. The lines can be divided into three groups from left to right as shown in Fig. 6. The first group ($P_{R,\parallel} \approx$ –0.3 a.u.) corresponds to the two-electron capture into the $2l2l'$ states while the argon recoils are in the ground state. The second group ($P_{R,\parallel} \approx$ 0.3 a.u.) and the third group ($P_{R,\parallel} \approx$ 0.8 a.u.) correspond to the two-electron capture into the $2l2l'$ states while the argon recoils are in singly excited $3s^23p^33d$ and $3s^23p^3nl$ ($n \geqslant 4$) states, respectively. The values of longitudinal momentum $P_{R,\parallel}$ for DECA with various electronic configurations are summarized in Table II (DECA columns). It is clear from the distribution that the two electrons are dominantly captured into the states with principal quantum number $n = 2$. These channels correspond to endothermic reactions; that is, more energies are required if the two electrons are captured into even higher doubly excited states (e.g., $n > 2$), and the possibility

TABLE II. Recoil ion longitudinal momenta $P_{R,\parallel}$. DECA is double-electron capture into the autoionizing states ($2s2s$, $2s2p$) with the target Ar^{2+} ion in the ground state and in various excited states. TDI is single-electron capture into projectile states of $n = 1$ and 2 with the target Ar^{2+} ions in the ground state and in various excited states. The first column lists recoil ion configurations. The energy-level data used for calculating Q values are taken from the NIST atomic spectra database [32].

| | $P_{R,\parallel}$ (a.u.) | | | |
| | DECA | | DTI | |
Ar^{2+} Config.	$2s2s$	$2s2p$	$n = 1$	$n = 2$
$3s^23p^4\,^3P_2$	–0.36	–0.34	–1.47	–0.11
$3s^23p^4\,^3P_{1,0}$	–0.35	–0.33	–1.46	–0.10
$3s^23p^4\,^1D_2$	–0.30	–0.28	–1.41	–0.05
$3s^23p^4\,^1S_0$	–0.22	–0.20	–1.33	0.03
$3s3p^5\,^3P^{\circ}_{2,1,0}$	0.12	0.13	–1.00	0.36
$3s3p^5\,^1P^{\circ}_1$	0.24	0.26	–0.87	0.49
$3s^23p^3(^4S^{\circ})3d$	0.25 to 0.30	0.26 to 0.31	–0.87 to –0.82	0.49 to 0.54
$3s^23p^3(^2D^{\circ})3d$	0.32 to 0.49	0.33 to 0.51	–0.80 to –0.62	0.50 to 0.74
$3s^23p^3(^2P^{\circ})3d$	0.37 to 0.52	0.38 to 0.54	–0.72 to –0.59	0.62 to 0.77
$3s^23p^3(^2D^{\circ})4l\,(l \geqslant 1)$	0.46 to 0.77	0.48 to 0.79	–0.65 to –0.34	0.71 to 1.02
$3s^23p^3(^4S^{\circ})4l\,(l \geqslant 1)$	0.49 to 0.69	0.51 to 0.71	–0.62 to –0.42	0.74 to 0.94
$3s^23p^3(^2P^{\circ})4l\,(l \geqslant 1)$	0.50 to 0.82	0.52 to 0.84	–0.61 to –0.29	0.75 to 1.07
$3s^23p^35s$	0.69 to 0.83	0.71 to 0.85	–0.42 to –0.28	0.94 to 1.08
Limit	1.01	1.02	–0.11	1.25
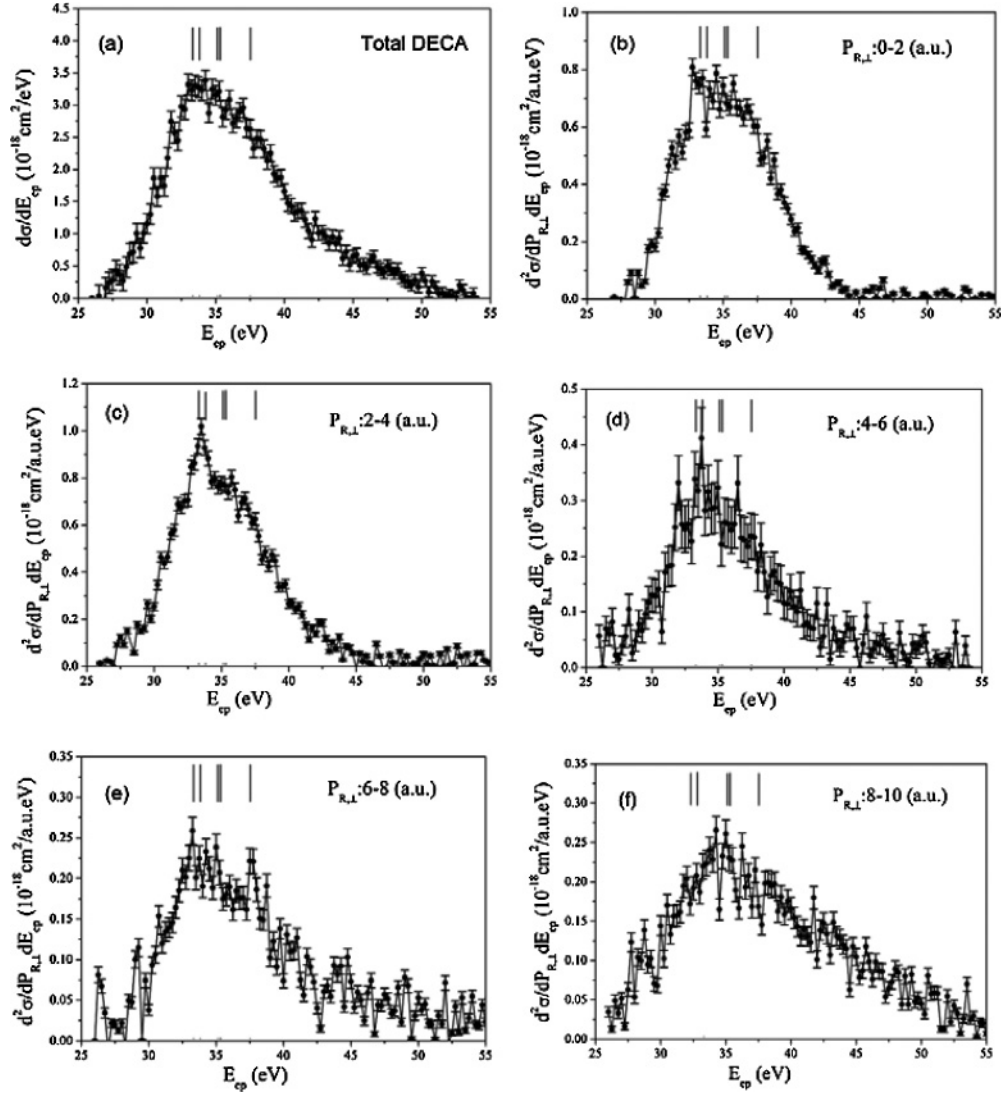
FIG. 7. Electron-energy spectra in the projectile frame at different transverse momenta with the continuum background subtracted. The short solid vertical lines are the Auger electron transitions from the $2l2l'$ states. (a) The total projectile Auger electron spectrum. (b)–(f) Individual spectra for transverse momentum intervals of $P_{R,\perp} = 0$–2, 2–4, 4–6, 6–8, and 8–10 a.u., respectively.

will become smaller. From the comparisons it can be concluded that the double-electron capture into the $2l2l'$ autoionizing states preferentially results in the recoil Ar^{2+} ions in the ground state and lowly excited states (see Table II).

For the direct transfer ionization process, the equation for the recoil ion longitudinal momentum can be written as [31]

$$P_{R,\parallel} = -\frac{Q}{v_P} - (m+1)\frac{v_P}{2} + \frac{E_{ep}}{v_P}, \qquad (5)$$

where m is the number of captured electrons and E_{ep} is the kinetic energy of the continuum electrons in the projectile frame. Accordingly, the recoil longitudinal momentum $P_{R,\parallel}$ in the two-dimensional plot has a linear relation to the E_{ep} [31]. The $P_{R,\parallel}$ value for E_{ep} at near zero directly reflects the electronic state of the captured electron. The two solid vertical longer black lines at $P_{R,\parallel} = -1.47$ a.u. and $P_{R,\parallel} = -0.11$ a.u. in the lower part of Fig. 6 correspond to the longitudinal momenta of the single-electron capture into the ground state and $n = 2$ states, respectively. In the DTI process, the recoil

ions can be left in various excited states, which will result in different $P_{R,\parallel}$. The short red line group ($P_{R,\parallel}$, ranging from -1.47 to -0.28 a.u.) and the short blue line group ($P_{R,\parallel}$, ranging from -0.11 to 1.25 a.u.) correspond to ground-state capture and $n = 2$ states capture with recoil ions in singly excited states, respectively. The corresponding $P_{R,\parallel}$ values are listed in Table II under the DTI column for various electronic configurations. In the present experiment, due to the large mass of Ar atoms, the momentum resolution of recoil ions is not high. Thus, the different lines cannot be resolved. From the analysis of the distribution and the lines in the two-dimensional plot, it can be seen that most of the events are scattered between the two longer vertical black lines. Thus, we can conclude that, for DTI processes, the electron is preferentially captured into the ground state of the projectile, leaving the Ar^{2+} ions in various excited states.

By projecting the data in Fig. 6 to the electron-energy axis, the electron-energy spectrum in the projectile frame can be produced. Most of the intensity occurs at electron energies
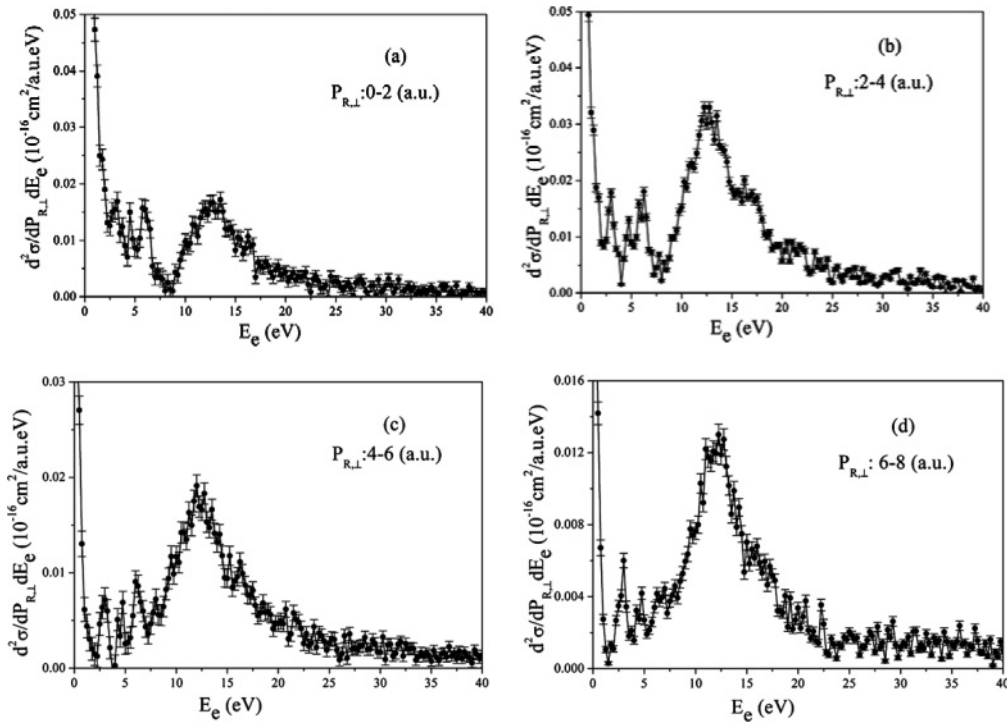
FIG. 8. The dependence of the target Auger transitions on the recoil ion transverse momenta $P_{R,\perp}$.

close to zero. A part of them corresponds to the process with one electron transferred into the bound state and one electron captured into the projectile continuum (ECC). The characteristics of the ECC electrons in TI process will be discussed in a forthcoming paper. Subtracting the continuum background, we obtain the energy distribution from the decay of the doubly excited states, which is shown in Fig. 7(a). The short vertical lines indicate the predicted positions of the decays for different $2l2l'$ states. In order to understand how the double-electron capture occurs, we investigate the dependence of the capture cross sections on the transverse momentum of the recoil ions, which reflects the collision distances between the projectile and the target nucleus in the interaction. The doubly differential cross sections $\frac{d^2\sigma}{dP_{R,\perp}dE_e}$ are shown in Figs. 7(b)–7(f) for recoil transverse momenta of $P_{R,\perp}$ = 0–2, 2–4, 4–6, 6–8, and 8–10 a.u., respectively. The production cross sections of the doubly excited states are significant for the transverse momenta less than 4 a.u. This indicates that, first, the doubly excited states through two-electron capture mainly occur at relatively small transverse momentum exchange. Second, as stated earlier, the target ions are left most probably in the ground states or in the lowly excited states. One possible reason for this is that the doubly excited states may not survive from violent interaction, which will result in more electron emissions and thus lead to other TI channels.

By subtracting the continuum background from the total electron-energy spectrum in the laboratory frame, we present the structure of the electron-energy spectrum at different transverse momenta in Figs. 8(a)–8(d). It can be seen that with the increase of the transverse momentum, the cross sections first go higher at $P_{R,\perp}$ = 2–4 a.u. and then become smaller, but the peak structure does not show any significant changes.

The results indicate that with one electron captured into the projectile, the population of target autoionizing states (here only one Auger decay will be activated) is similar within a broad range of collision distances. The excitation of the target ions in SECA is more effective at $P_{R,\perp}$ = 2–4 a.u. As mentioned earlier, the capture leads to the intermediate autoionizing states of $Ar^+([Ne]3s3p^5nl)$. By comparing the results of Figs. 7 and 8, it is clear that double-electron capture to the autoionizing states has relatively larger cross sections over the SECA process. One possible reason is that the DEC process involves the outer-orbital two $3p$ electrons while the SEC involves the $3s$ electron, and also the binding energies and orbital radii of $3s$ and $3p$ are obviously different.
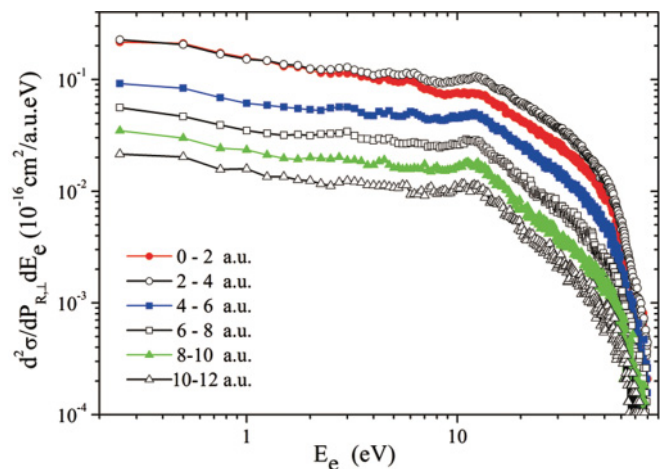

FIG. 9. (Color online) The dependence of the electron production on the recoil ion transverse momentum. The selected intervals of the recoil transverse momentum are indicated in the legend.

The total electron production from DTI at different transverse momentum intervals have been studied as well. The doubly differential cross sections of the electron emission are drawn in Fig. 9 for recoil transverse momenta of $P_{R,\perp} = 0$–2, 2–4, 4–6, 6–8, 8–10, and 10–12 a.u. For each selected transverse momentum range, the curves show similar dependence with the increasing electron energy. Obviously, the electron production is the highest for the small transverse momenta (0–4 a.u.), which means that most of the continuum electrons are produced at large collision distances. In the transverse momentum ranges of 0–2 and 2–4 a.u., the production cross section (PCS) is almost the same for the electron energies less than 2 eV. However, when the electron energy is larger than 2 eV, the PCS (open circles) for $P_{R,\perp} = 2$–4 a.u. becomes significantly larger than that for $P_{R,\perp} = 0$–2 a.u. (solid circles). This indicates that in the DTI process, the production of the low energy electrons ($E_e < 1$ eV) is relatively higher at small transverse momentum. The similarity of the curves at different transverse recoil ion momenta shows that the DTI mechanism plays the dominant role in the continuum electron production.

IV. SUMMARY

A kinematically complete experiment was performed using reaction microscope to investigate the electron emission from the single-electron capture with simultaneous single ionization of target atom in 30 keV/u He^{2+} on argon. The electron momentum distribution shows a pattern different than the one of the symmetric collisions system (He^{2+} on He). An intensive peak for the electrons with near-zero kinetic energies has been observed. It is demonstrated that the mechanisms of direct transfer ionization, double-electron capture with autoionization, and single-electron capture with autoionization of target contribute to the electron emission. Comparison of resonance energies shows that the resonant structures in the electron energy spectrum can be attributed to the Auger decays of the autoionizing states of the recoil ions Ar^{+**} and scattered He^{**}. The SECA proceeds via transferring one $3s$ electron and exciting one $3p$ electron into the $3d$ or $4l$ orbitals, which yields autoionization states Ar^+ ([Ne]$3s3p^5nl$, $nl = 3d,4s,4p,4d$). The double-electron capture into the projectile mainly populates the $2l2l'$ states, and most DEC electrons are produced at small transverse momentum of recoil ions. In the presently studied transfer ionization channel, the DTI process dominates the electron emission, and the DTI electron emission contributes greatly at small transverse momentum. There is no evidence that the saddle point electron mechanism plays any role. Extensive theoretical investigations are needed to describe the observed phenomenon.

[1] N. V. Maydanyuk, A. Hasan, M. Foster, B. Tooke, E. Nanni, D. H. Madison, and M. Schulz, Phys. Rev. Lett. **94**, 243201 (2005).

[2] M. Schulz, A. Hasan, N. V. Maydanyuk, M. Foster, B. Tooke, and D. H. Madison, Phys. Rev. A **73**, 062704 (2006).

[3] A. Hasan, N. V. Maydanyuk, B. Fendler, A. Voitkiv, B. Najjari, and M. Schulz, J. Phys. B: At. Mol. Opt. Phys. **37**, 1923 (2004).

[4] R. Moshammer *et al.*, Phys. Rev. Lett. **79**, 3621 (1997).

[5] M. Schulz, R. Moshammer, D. Fischer, H. Kollmus, D. H. Madison, S. Jones, and J. Ullrich, Nature (London) **422**, 48 (2003).

[6] J. H. McGuire, *Electron Correlation Dynamics in Atomic Collisions* (Cambridge University Press, Cambridge, 1997).

[7] H. Schmidt-Böcking, V. Mergel, L. Schmidt, R. Dörner, O. Jagutzki, K. Ullmann, T. Weber, H. J. Lüdde, E. Weigold, and A. S. Kheifets, Radiat. Phys. Chem. **68**, 41 (2003).

[8] V. Mergel *et al.*, Phys. Rev. Lett. **79**, 387 (1997).

[9] R. Dörner, V. Mergel, O. Jagutzki, L. Spieberger, J. Ullrich, R. Moshammer, and H. Schmidt-Böcking, Phys. Rep. **330**, 95 (2000).

[10] J. Ullrich, R. Moshammer, A. Dorn, R. Dörner, L. Ph. H. Schmidt, and H. Schmidt-Böcking, Rep. Prog. Phys. **66**, 1463 (2003).

[11] V. Mergel, R. Dörner, K. Khayyat, M. Achler, T. Weber, O. Jagutzki, H. J. Lüdde, C. L. Cocke, and H. Schmidt-Böcking, Phys. Rev. Lett. **86**, 2257 (2001).

[12] M. A. Abdallah, W. Wolff, H. E. Wolf, L. F. S. Coelho, C. L. Cocke, and M. Stöckli, Phys. Rev. A **62**, 012711 (2000).

[13] L. Ph. H. Schmidt, M. S. Schöffler, K. E. Stiebing, H. Schmidt-Böcking, R. Dörner, F. Afaneh, and Th. Weber, Phys. Rev. A **76**, 012703 (2007).

[14] R. D. DuBois, Phys. Rev. A **36**, 2585 (1987).

[15] W. Groh, A. S. Schalchter, A. Müller, and E. Salzborn, J. Phys. B: At. Mol. Opt. **15**, L207 (1982).

[16] P. Moretto-Capelle, D. Bordenave-Montesquieu, A. Bordenave-Montesquieu, and M. Benhenni, J. Phys. B: At. Mol. Opt. **31**, L423 (1998).

[17] L. Vikor, L. Sarkadi, J. A. Tanis, A. Bader, P. A. Zavodszky, M. Kuzel, K. Groeneveld, and D. Berenyi, Nucl. Instrum. Methods Phys. Res., Sect. B **124**, 342 (1997).

[18] D. Fregenal, J. Fiol, G. Bernardi, S. Suárez, P. Focke, A. D. González, A. Muthig, T. Jalowy, K. O. Groeneveld, and H. Luna, Phys. Rev. A **62**, 012703 (2000).

[19] A. L. Godunov, C. T. Whelan, and H. R. J. Walters, J. Phys. B: At. Mol. Opt. Phys. **37**, L201 (2004).

[20] X. Ma *et al.*, J. Phys.: Conf. Ser. **163**, 012104 (2009).

[21] X. Ma, X. L. Zhu, H. P. Liu, B. Li, S. F. Zhang, S. P. Cao, W. T. Feng, and S. Xu, Sci. China, Series G **51**, 755 (2008).

[22] X. L. Zhu, X. Ma, B. Li, S. F. Zhang, W. T. Feng, H. P. Liu, L. F. Chen, S. P. Cao, D. B. Qian, and D. C. Zhang, J. Phys.: Conf. Ser. **163**, 012064 (2009).

[23] O. Jagutzki, V. Mergel, K. Ullmann-Pfleger, L. Spielberger, U. Meyer, R. Dörner, and H. Schmidt-Böcking, *Imaging*

Spectrometry IV, edited by M. R. Descour and S. S. Shen, Proceedings of SPIE Vol. **3438**, 322 (1998).

[24] D. L. Guo *et al.*, Acta Physics Sinica **60** (2011).

[25] R. E. Olson, Phys. Rev. A **33**, 4397 (1986).

[26] R. E. Olson, T. J. Gay, H. G. Berry, E. B. Hale, and V. D. Irby, Phys. Rev. Lett. **59**, 36 (1987).

[27] R. E. Olson, C. R. Feeler, C. J. Wood, C. L. Cocke, R. Dörner, V. Mergel, H. Schmidt-Böcking, and J. Ullrich, Nucl. Instrum. Methods Phys. Res., Sect. B **124**, 249 (1997); R. E. Olson, **27**, 1871 (1983).

[28] F. Afaneh, R. Dörner, L. Schmidt, Th. Weber, K. E. Stiebing, O. Jagutzki, and H. Schmidt-Böcking, J. Phys. B: At. Mol. Opt. Phys. **35**, L229 (2002).

[29] Th. Weber *et al.*, J. Phys. B: At. Mol. Opt. Phys. **33**, 3331 (2000).

[30] R. Moshammer *et al.*, Phys. Rev. Lett. **73**, 3371 (1994).

[31] L. Ph. H. Schmidt, F. Afaneh, M. Schöffler, J. Titze, O. Jagtzki, Th. Weber, K. E. Stiebing, R. Dörner, and H. Schmidt-Böcking, Phys. Scr., T **110**, 379 (2004).

[32] [http://physics.nist.gov/PhysRefData/ASD/].